

Surface-Aware Distilled 3D Semantic Features

Lukas Uzolas Elmar Eisemann Petr Kellnhofer
Delft University of Technology
The Netherlands

{l.uzolas, e.eisemann, p.kellnhofer}@tudelft.nl

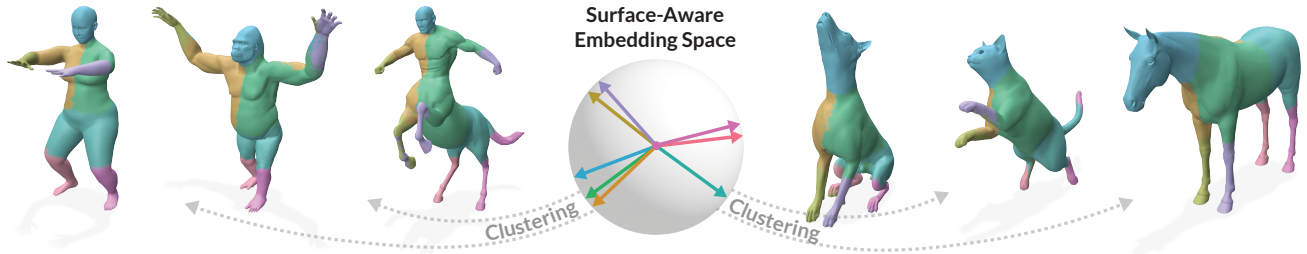


Figure 1. We introduce a *surface-aware* feature embedding space separating instances of the same semantic class (e.g. right vs. left instances for “hand/paw”). Our method implicitly aligns semantically-related regions (shown with same colors) across diverse 3D shapes in a self-supervised manner without access to any correspondence labels. See Sec. 6.1 for figure details. The project site is available at: <https://lukas.uzolas.com/SurfaceAware3DFeaturesSite>.

Abstract

Many 3D tasks such as pose alignment, animation, motion transfer, and 3D reconstruction rely on establishing correspondences between 3D shapes. This challenge has recently been approached by matching of semantic features from pre-trained vision models. However, despite their power, these features struggle to differentiate instances of the same semantic class such as “left hand” versus “right hand” which leads to substantial mapping errors. To solve this, we learn a surface-aware embedding space that is robust to these ambiguities. Importantly, our approach is self-supervised and requires only a small number of unpaired training meshes to infer features for new 3D shapes at test time. We achieve this by introducing a contrastive loss that preserves the semantic content of the features distilled from foundational models while disambiguating features located far apart on the shape’s surface. We observe superior performance in correspondence matching benchmarks and enable downstream applications including in-part segmentation, pose alignment, and motion transfer.

1. Introduction

Establishing accurate correspondence between 3D shapes is important in many applications, including 3D registra-

tion, pose alignment, motion transfer, as well as static and dynamic 3D reconstruction. Historically, geometric descriptors have been used to determine matches between 3D shapes under isometric deformations, but they struggle with non-isometric deformations [5, 72, 76]. In contrast, neural features, stemming from pre-trained 2D vision models, have recently achieved great success in identifying correspondences between vastly different shapes [51, 75, 81, 92], such as mapping from cats to lions.

Despite this inter-class robustness, neural features often struggle to disambiguate between instances of the same class like “left hand” and “right hand” (see Fig. 6). Such mismatches can lead to substantial errors in downstream applications (see Sec. 6.2). Recent research has demonstrated that these features contain global pose information and that disambiguation is possible in a 2D scenario [91]. However, achieving the same effect on distilled 3D features is not trivial, especially in a low-data regime, which is prevalent in 3D, where data acquisition and labeling is difficult.

Our work improves 3D neural features distilled from pre-trained 2D vision models by embedding them into a space disambiguating intraclass instances. We achieve this without large annotated datasets using a self-supervised learning scheme guided by in-shape geodesic distances without the need for shape pairs. Training with a limited number of 3D meshes, our method produces *surface-aware features* for diverse new shapes. In quantitative and qualitative com-

parisons to prior work, we demonstrate superior suitability of these features to serve as robust descriptors for matching and as building blocks for solving other tasks.

In summary, we make the following contributions: 1. We introduce a novel contrastive loss for self-supervised distillation of 3D features. 2. We demonstrate the effectiveness of our surface-aware features in multiple experiments and correspondence matching benchmarks. 3. We showcase two additional downstream applications that motivate further future use cases.

2. Related Works

Our method utilizes contrastive learning to improve semantic features extracted from foundational models for robust 3D shape correspondence matching. In this section, we discuss prior work in these three areas.

2.1. Shape correspondences

Point-to-Point Classical shape registration methods directly minimize global [7] or local [9] inter-shape distances making them susceptible to local minima [85]. This motivates the design of more informative local geometric descriptors [5, 72, 76]. These can alternatively be learned [16, 36] from voxelized patches [4, 33, 88] or from point clouds [19–21, 28, 87]. The learning can be supervised by labels [16] or achieved without them [28, 35, 44, 89]. Our method falls into the latter category, as our contrastive loss motivates our encoder to separate instances by approximating geodesic distances [83] without training data labels. This is conceptually similar to previous methods for near-isometric shape deformations [38, 54, 67]. However, we distinctly do not measure geodesic distortions between shape pairs, and therefore we do not limit our method to isometric deformations, and we do not compute any geodesics during inference. Instead, we only use the geodesics to disambiguate information already available in the image-based features, which is critical for our results.

The correspondences can be recovered from descriptors by a matching [31], directly regressed [50, 79] or established on parametric templates [22, 35]. Instead, we focus on the descriptors themselves, and we show several different application scenarios in Sec. 6.

Surface mapping Functional Maps (FMs) [58] allow for matching on a surface. FMs are real-valued surface functions in the space of Laplace-Bertrami eigenfunctions, supporting linear transformations between shapes. Constrained to match surface descriptors for each shape [5, 72, 76] they allow extracting point-wise correspondences [58, 63]. These functions can also be learned [46] often with little or no supervision [23, 32, 38, 65, 73]. Extrinsic alignment can support nonisotropic deformations [26, 27]. In this work,

we focus on improving features for direct point-to-point matching in the spatial domain, but previous work demonstrated promising results when combining similar image-based features with FMs [24, 55].

2.2. Image-based features for 3D shapes

Image-based features emerge in large visual models for 2D image tasks. Self-supervised features from Vision Transformers such as DINO-ViT [12] and DINOv2 [57] locally encode semantic information useful for segmentation [12] or image-to-image correspondence matching [2]. SD-DINO [90] adds complementary features from the diffusion-based image synthesis model Stable Diffusion [64]. Lifting these features to 3D has enabled the self-supervised construction of canonical surface maps [70], transfer of appearance between 3D shapes [30], 3D animation [78], keypoint detection [81] or matching of surface correspondences [14, 24, 55]. However, despite their semantic versatility, disambiguating between intraclass instances, such as left and right hands, remains challenging but possible, as shown in a recent 2D image study [91] This motivates our 3D shape descriptors for resolving instance ambiguity. We evaluate the Diff3F features [24] as a basis for our autoencoded embedding. We then use geodesics as a guiding signal, which is conceptually similar to the concurrent work [14]. However, we demonstrate that our distinct design choices lead to better performance in Sec. 5.3. Moreover, our method is purely intrinsic and does not require aligned mesh pairs for training.

Beyond vision-only models, multimodal large language models have recently been effective in image and 3D shape analysis including keypoint labeling [34] and shape co-segmentation [1]. In our work, we focus on vision-only models because of their simplicity, but we consider a model combination a promising research direction.

2.3. Contrastive Learning

Contrastive learning embeds similar samples close to each other while keeping dissimilar samples apart. This can be achieved directly by minimizing and maximizing embedding distances for positive and negative pair samples, respectively [15, 37, 66, 80] or indirectly, such as by optimizing performance in an auto-regressive task [56]. Training pairs can be obtained by data augmentation [13], from memory banks [40, 82], or by clustering [10, 11]. Learning with cross-domain labels yields joint embeddings, as demonstrated by CLIP [62] for text and images. We design our contrastive loss to disambiguate intraclass instances guided by a geodesic metric.

3. Preliminaries

We built upon methods that aggregate features from pre-trained 2D vision models on 3D meshes [14, 24, 55, 81]. In

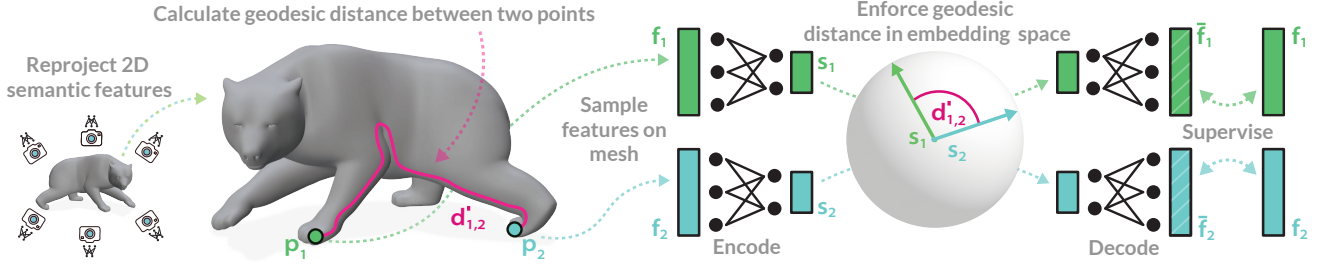


Figure 2. Overview of our method. We feed images of a 3D shape rendered from multiple viewpoints to a pre-trained 2D vision model and extract features that are then projected back onto surface points \mathbf{p}_i and aggregated into per-point features \mathbf{f}_i (Sec. 3). Next, we point-wise embed the *base features* \mathbf{f}_i into our *surface-aware features* \mathbf{s}_i residing in a lower-dimensional space learned using our contrastive loss preserving geodesic distances $d_{i,j}$ and a reconstruction loss matching decoded features $\tilde{\mathbf{f}}_i$ to \mathbf{f}_i (Sec. 4). The *surface-aware features* \mathbf{s}_i serve as robust descriptors for correspondence matching (Sec. 5) and base blocks for other tasks (Sec. 6).

this section, we give a brief overview on these methods.

3.1. Reprojection of 2D Features

We represent a 3D shape as a triangular mesh with a tuple of N vertices and M triangular faces, that is, $\mathcal{M} := (\{\mathbf{p}_n \in \mathbb{R}^3 | n = 1, \dots, N\}, \{\mathbf{t}_m \in \mathbb{N}^3 | m = 1, \dots, M\})$. The rendering function $R_{rgb} : (\mathcal{M}, \mathcal{C}) \rightarrow \mathbf{I}_{rgb}$ projects \mathcal{M} into a camera \mathcal{C} and outputs an image $\mathbf{I}_{rgb} \in \mathbb{R}^{H \times W \times 3}$, with height H and width W . Optionally, texturing is possible in $R_{rgb}(\cdot)$ or as a ControlNet [93] post-processing. The image is then passed to a pre-trained vision model [12, 57, 64, 90] to obtain dense semantic feature maps $\mathbf{F} \in \mathbb{R}^{h \times w \times f}$ with h, w, f as two spatial and one feature dimension. Finally, per-vertex features $\mathbf{f}_n \in \mathbb{R}^f$ are obtained by projective texture mapping of \mathbf{F} onto \mathcal{M} . To cover the whole surface, features are aggregated across multiple cameras, resulting in a set of features $\mathcal{F}_{\mathcal{M}} := \{\mathbf{f}_n \in \mathbb{R}^f | n = 1, \dots, N\}$. Throughout this work, we refer to $\mathcal{F}_{\mathcal{M}}$ as the *base features* on which our method is built. The exact choice of $\mathcal{F}_{\mathcal{M}}$ is orthogonal to our contribution but must encode semantic information. To this extent, we use Diff3F [24] in this work.

Correspondence Matching Features $\mathcal{F}_{\mathcal{M}}$ have been shown to encode strong semantic information useful for correspondence matching [24, 75]. In the simplest case, the feature $\mathbf{f}_n \in \mathcal{F}_{\mathcal{T}}$ of a target mesh \mathcal{T} that best matches the feature $\mathbf{f}_m \in \mathcal{F}_{\mathcal{S}}$ of a source mesh \mathcal{S} is determined by maximizing the cosine similarity $\phi : \mathbb{R}^f \times \mathbb{R}^f \rightarrow \mathbb{R}$:

$$\phi(\mathbf{f}_i, \mathbf{f}_j) = \frac{\mathbf{f}_i^T \mathbf{f}_j}{\|\mathbf{f}_i\|_2 \|\mathbf{f}_j\|_2}, \quad (1)$$

such that $\tau(\mathbf{p}_m) = \arg \max_{\mathbf{p}_n} \phi(\mathbf{p}_n \rightarrow \mathbf{f}_n, \mathbf{p}_m \rightarrow \mathbf{f}_m)$ is the best matching point. However, the features $\mathcal{F}_{\mathcal{M}}$ do not differentiate between semantic instances well (see Fig. 5) which we address by learning robust *surface-aware features* $\mathcal{S}_{\mathcal{M}}$.

4. Method

Our goal is to learn an embedding resolving instance ambiguities of the *base features* $\mathcal{F}_{\mathcal{M}}$ and obtain *surface-aware features* $\mathcal{S}_{\mathcal{M}}$ (see Fig. 2). We achieve this by training a point-based feature auto-encoder with a limited set of training meshes and our contrastive loss for self-supervision. At test time, we can produce *surface-aware features* for novel unseen shapes without additional fine-tuning.

4.1. Setup

Our method requires a potentially small set of training meshes $\mathbf{M}_t = \{\mathcal{M}_i | i = 1, \dots, K\}$, each associated with *base features* $\mathcal{F}_{\mathcal{M}}$ obtained following Sec. 3 and normalized by a Euclidean norm such that $\forall \mathbf{f}_n \in \mathcal{F}_{\mathcal{M}}, \|\mathbf{f}_n\|_2 := 1$.

Unlike other approaches [21, 41], our method does not require canonical mesh alignment [41], nor rely on its estimation [21] because it purely uses intrinsic mesh properties rather than absolute vertex position. Similar considerations were made by prior methods based on Functional maps [58]. Furthermore, our encoder is point-based and does not take into account global shape and connectivity. Both of these design choices favor generalization under transformations ranging from coordinate swap to shape reposing.

4.2. Separating Front Paw from Back Paw

Our embedding aims to separate multiple instances of the same class that are difficult to directly disambiguate in $\mathcal{F}_{\mathcal{M}}$. For example, consider the two surface points, \mathbf{p}_1 and \mathbf{p}_2 , on the bear’s paws in Fig. 2. The prevalent semantic significance of the “paw” concept hinders the separability of the corresponding *base features* \mathbf{f}_1 and \mathbf{f}_2 . Fig. 6 illustrates this for human arms and Diff3F features [24]. To solve this, we train a point-wise feature autoencoder, producing our *surface-aware features* $\mathcal{S}_{\mathcal{M}} \subset \mathbb{R}^s$ in its embedding space. We motivate the feasibility of separation by the prior observations that vision features additionally carry informa-

tion about the global pose [91]. We postulate that this enables our model to distinguish between part instances when guided by their intrinsic distance. We adopt the geodesic distance $d_{1,2}$ between \mathbf{p}_1 and \mathbf{p}_2 for this purpose. Following contrastive learning, we sample point pairs to enforce $\phi(\mathbf{s}_1, \mathbf{s}_2) \approx d_{1,2}$ for $\mathbf{s}_n \in \mathcal{S}_{\mathcal{M}}$. We validate our choice of hyperspherical embedding space against Euclidean space in Sec. 5.3.

Model We train a *base feature* encoder \mathcal{E} , such that $\mathbf{s}_n = \mathcal{E}(\mathbf{f}_n)/\|\mathcal{E}(\mathbf{f}_n)\|_2$ is *surface-aware feature* $\mathbf{s}_n \in \mathbb{R}^s$ in a hypersphere embedding. During training, we randomly sample a training mesh $\mathcal{M} \in \mathbf{M}_t$ with *base features* $\mathcal{F}_{\mathcal{M}}$, which we encode pointwise to obtain $\mathcal{S}_{\mathcal{M}}$.

In each training iteration, we use furthest-point sampling to choose a random subset of A anchor points \mathbf{p}_a among the mesh vertices $\mathbf{p}_i \in \mathcal{M}$ and compute geodesic distances $d_{n,a}$ for each pair of a mesh and anchor point. We additionally rescale $d_{n,a}$ to a maximum of one, such that $d'_{n,a} := d_{n,a}/\max_{n,a}(d_{n,a})$, which removes the dependency on the scale of the mesh.

From here, our contrastive loss enforces preservation of the geodesic distances in the embedding space:

$$\mathcal{L}_c = \frac{1}{NA} \sum_n^N \sum_a^A |d'_{n,a} - \left(1 - \frac{\phi(\mathbf{s}_n, \mathbf{s}_a)}{2}\right)|. \quad (2)$$

The loss operates in a hyperspherical embedding space and utilizes cosine similarity mapped to the $[0, 1]$ range. Hereby, \mathcal{L}_c penalizes features close in the embedding space but distant on the shape surface and vice versa.

Furthermore, we found it beneficial for the preservation of semantic information to train a feature decoder $\bar{\mathbf{f}}_n = \mathcal{D}(\mathbf{s}_n)/\|\mathcal{D}(\mathbf{s}_n)\|_2$ in an autoencoder fashion. To this extent, we utilize a reconstruction loss:

$$\mathcal{L}_r = \frac{1}{N} \sum_n 1 - \phi(\mathbf{f}_n, \bar{\mathbf{f}}_n). \quad (3)$$

We train both the encoder and the decoder end-to-end with the combined loss $\mathcal{L} = w_r \mathcal{L}_r + w_c \mathcal{L}_c$, where a choice $w_r = w_c = 1$ works well in our tests. We do not observe an increase in performance with a higher w_c .

Note that our training procedure, in contrast to related works [14, 21, 44], does not require target and source pairs.

4.3. Implementation

During preprocessing, we rasterize our triangular meshes and precompute *base features* for all vertices following Sec. 3. We implement our autoencoder in PyTorch2 [3]. The encoder \mathcal{E} is a Multilayer Perceptron consisting of three blocks, where each block has two linear layers, SiLU activation [29], and layer normalization [6]. The first layer in each block employs a skip connection [39], while the

second reduces the dimensionality by a factor of two. For Diff3F [24] as *base features*, the dimensionality is reduced from $f = 2048$ to $s = 256$. The decoder \mathcal{D} is a mirrored copy of the encoder. We train our model on NVIDIA RTX 3090 for 50k iterations with the AdamW optimizer [49] and a learning rate of 0.0001 that take ≈ 2 hours.

We choose an exponential moving average [60] of the model with the lowest validation loss, without the need for any correspondence labels. Geodesic distances are calculated on the fly with the heat method [17] implemented in Geometry Central [68] and we use the Polyscope renderer [69] for visualization.

5. Experiments

We evaluate the performance of our *surface-aware features* in 3D correspondence matching, and in a downstream inference task of skinning weight regression.

5.1. Point-to-Point Correspondence Matching

We follow the evaluation setup of Diff3F [24] and assess our *surface-aware features* in a correspondence matching task on human and animal shapes.

Data We train a single autoencoder on a joint dataset consisting of 49 animal samples from the *SMAL* dataset [94] and 49 humans from the *SURREAL* dataset [35]. We choose 2 from each dataset for validation. For testing we use re-meshed versions of humans from *SHREC'19* [23, 53] and animals from both *SHREC'20* [25] and the animal-only subset of *TOSCA* [8].

Baselines We compare our method against the unsupervised image-based Diff3F method [24], which also provides our *base features*, and against 3DCODED [35], DPC [44] and SE-OrNet [21], which have been trained on thousands of samples, while our method is trained on less than 100 samples.

Metrics We report commonly used point correspondence metrics for 1024 points per mesh [21, 24, 35, 44]¹. The correspondence error measures a distance between the computed correspondence point $\tau(\mathbf{p}_n)$ (see Sec. 3) and the ground-truth correspondence point \mathbf{t}_n^{gt} : $err = \frac{1}{n} \sum_{\mathbf{p}_n \in \mathcal{S}} \|\tau(\mathbf{p}_n) - \mathbf{t}_n^{gt}\|_2^2$. The accuracy is the fraction of points with an error below a threshold $\epsilon \in [0, 1]$: $acc(\epsilon) = \frac{1}{n} \sum_{\mathbf{p}_n \in \mathcal{S}} \mathbb{I}(\|\tau(\mathbf{p}_n) - \mathbf{t}_n^{gt}\|_2 < \epsilon g)$, where g is the maximal Euclidean distance in the target shape and $\mathbb{I}(\cdot)$ is the indicator function.

¹We use the provided code and validate that we follow the same experimental procedure and metric definitions.

		SHREC'19	TOSCA	SHREC'20
3DC†	err ↓	8.10	19.20	x
	acc ↑	2.10	0.50	x
DPC†	err ↓	6.26	3.74	<u>2.13</u>
	acc ↑	17.40	30.79	31.08
SEN†	err ↓	4.56	4.32	1.00
	acc ↑	21.41	33.25	31.70
Diff3F*	err ↓	1.69±1.44	4.51±5.48	5.34±10.22
	acc ↑	<u>26.25±9.30</u>	<u>31.00±15.73</u>	<u>69.50±24.99</u>
Ours	err ↓	0.43±0.76	1.65±2.15	3.89±8.90
	acc ↑	28.78±9.30	29.35±14.53	73.97±26.47

Table 1. Comparison of our 3D correspondence matching to prior works 3DC (3D-CODED [35]), DPC [44], SEN (SE-OrNet [21]), and Diff3F [24]. †) Numbers originate from [24], *) Experiments were replicated. Accuracy is for the commonly used $\epsilon = 1\%$. The per-column best results are bold and the second-to-best are underlined.

Results We provide quantitative results in Tbl. 5.1 and qualitative comparisons in Fig. 5. We find that our method achieves the lowest error on *SHREC'19* and *TOSCA*, despite being trained on fewer samples than the supervised baselines. Furthermore, we outperform the Diff3F *base features* on both *SHREC* datasets in terms of accuracy. While Diff3F achieves a higher accuracy at 1% threshold in *TOSCA*, Fig. 4 shows that the accuracy of our model is higher for thresholds above $\approx 2\%$. This suggests that our method excels in the removal of outliers that can be caused by mismatched components.

Fig. 5 shows that Diff3F struggles to separate intraclass instances such as left and right legs. In contrast, the results confirm the effectiveness of our contrastive loss in mitigating this issue. We observe the same behavior for *SHREC'20* in Fig. 3, which contains highly diverse animal shapes. Furthermore, our method generally produces visually smoother results (see Appendix 10.1 and the supplementary video).

5.2. Exploration of Embedding Space

To illustrate the effect of our contrastive loss on feature separation and downstream applications, we compare the 2D projections of the DIFF3F *base features* with our *surface-aware features*, and we evaluate both as a base for the prediction of skinning weights.

Setup We use our model, trained in Sec. 5.1, and create two dataset *SMPL^{eval}* and *SMAL^{eval}*. The former consists of 50 randomly-sampled *SMPL* [8] shapes and poses from *AMASS* [52], while the latter consists of 50 randomly-sampled *SMAL* [94] shapes in canonical poses.

Embedding We project Diff3F features aggregated from *SMPL^{eval}* to two dimensions using principal component

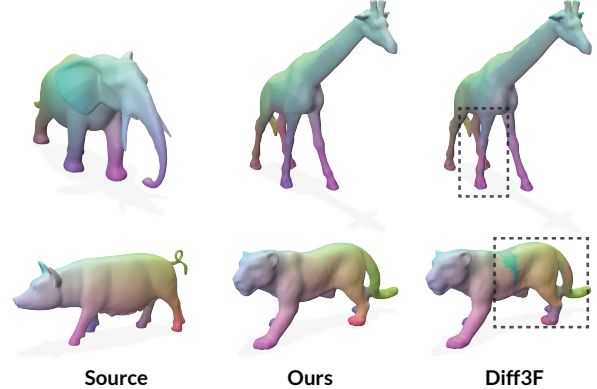


Figure 3. Qualitative comparison of correspondence matching on *TOSCA* (dense ground truth labels not available). Source shape (left) matched to target (right) using our and Diff3F features.

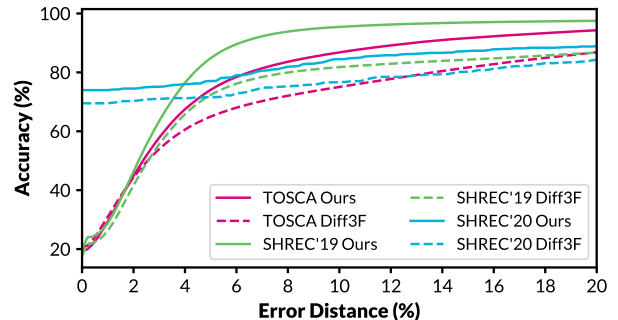


Figure 4. Correspondence accuracy (\uparrow is better) at different error distance thresholds for our own and Diff3F features.

analysis (PCA). In Fig. 6, we visualize the projection for two selected shapes from the same dataset. We repeat this with our *surface-aware features*. To avoid bias, we derive the visualized colors from the true SMPL [48] skinning weights $w_n \in \mathbb{R}^B$ for both methods, where B is the skinning weight dimension. We repeat this process for *SMAL^{eval}*. In Fig. 6, we see that our method yields an interpretable embedding that separates the leg and hand instances for animals and humans despite not having access to extrinsic (x, y, z) point positions. This remains a challenge for the Diff3F *base features*.

Downstream inference Furthermore, we train a simple regressor to predict skinning weights of a kinematic model in a one-shot setup. The pointwise regressor $\mathcal{W}_s(s_n)$ consists of a linear layer and a Softmax activation and regresses skinning weights \bar{w}_n from our *surface-aware features* or, in case of $\mathcal{W}_f(f_n)$, from the *base features*. We train both models fivefold supervised with the Mean Squared Error (MSE) and true weights separately on the *SMPL^{eval}* and *SMAL^{eval}* datasets, and we report test MSE for the remaining unused



Figure 5. Qualitative Comparison on the *SHREC'19* and *TOSCA* datasets with dense true correspondence labels. We show the source and target meshes with their ground truth correspondence labels (two left-most columns) in comparison to correspondences computed using our *surface-aware features* (forth column) and *Diff3F base features* (right-most column). We further highlight the correspondence error on the mesh surface (third and fifth column). The error colormap is normalized per sample by the maximal error over both methods to keep the error scale comparable across columns but not across rows. Our *surface-aware features* notably improve separation of the limb instances.

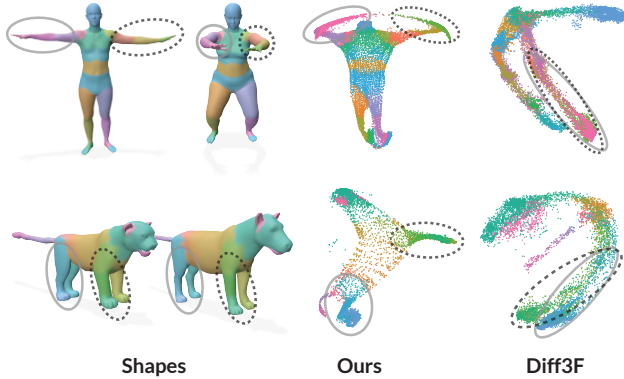


Figure 6. Two shapes (left) and a PCA-based 2D projections of their aggregated Diff3F *base features* and our *surface-aware features* (right). Notice the separation of limbs in our result compared to Diff3F. Our features originate from the same encoder for both shapes.

	$SMPL^{eval}$	$SMAL^{eval}$
Ours	.0014±.0006	.0048±.0008
Diff3F	.0058±.0024	.0086±.0028

Figure 7. Mean Squared Error of skinning weight regression (\downarrow is better) and its distribution across SMPL mesh surface.

samples in the source datasets (see Fig. 7). Our features achieve lower errors and exhibit better robustness to instance ambiguities.

5.3. Ablations

We motivate our design choices by ablation of various parts of our method in Tbl. 2 following the setup of Sec. 5.1.

Choice of Angular Space We demonstrate the effectiveness of our hyperspherical embedding by replacing our contrastive loss \mathcal{L}_c (Eq. 4.2) with three different options inspired by related work (see Appendix 8.2). First, the Relative Geodesic Loss (RGL) [41] optimizes relative distances in a Euclidean embedding. Similarly, the Naive Geodesic Loss (NGL) minimizes absolute distances. Finally, the Geometrical Similarity Loss (GSL) [14] enforces similarity of feature and surface distances in a local neighborhood. We remove feature and geodesic normalization wherever absolute magnitude needs to be learned. In Tbl. 2 (top), we observe that, except for correspondence accuracy for TOSCA, our contrastive loss \mathcal{L}_c outperforms either of the alternatives in the correspondence matching task.

		SHREC'19	TOSCA	SHREC'20
RGL	err \downarrow	0.80±1.08	2.74±2.53	5.29±9.85
	acc \uparrow	20.16±10.03	16.53±10.41	55.23±21.93
NGL	err \downarrow	0.54±0.90	2.11±2.02	4.86±9.49
	acc \uparrow	18.84±9.59	18.86±11.50	58.97±23.12
GSL	err \downarrow	1.72±1.45	4.17±5.21	4.34±9.23
	acc \uparrow	<u>26.89±9.07</u>	29.77±14.92	<u>73.39±26.31</u>
Diff3F	err \downarrow	1.69±1.44	4.51±5.48	5.34±10.22
	acc \uparrow	26.25±9.30	31.00±15.73	69.50±24.99
only \mathcal{L}_r	err \downarrow	1.65±1.44	4.70±5.64	4.87±9.38
	acc \uparrow	26.53±9.19	<u>30.27±15.17</u>	72.94±26.21
only \mathcal{L}_c	err \downarrow	0.38±0.61	<u>1.67±2.29</u>	<u>4.30±9.31</u>
	acc \uparrow	26.21±8.78	25.58±13.88	70.08±25.17
Ours	err \downarrow	0.43±0.76	1.65±2.15	3.89±8.90
	acc \uparrow	28.78±9.30	29.35±14.53	73.97±26.47

Table 2. Ablation of our method. *Above the bar*: Ablation of alternative losses inspired by related work [14, 41] compared to the unmodified Diff3F features. *Below the bar*: Our full method compared to its reduced variant omitting losses \mathcal{L}_c or \mathcal{L}_r . The per-column best results are bold and the second-to-best are underlined.

Contrastive and Reconstruction Loss In Tbl. 2 (bottom), we individually assess our two losses. We see that the performance with only the reconstruction loss \mathcal{L}_r is close to Diff3F. This indicates that the gain in performance does not originate predominantly from a smaller embedding space or from access to training data. Similarly, the contrastive loss \mathcal{L}_c alone results in an accuracy drop compared to our full model. This justifies our autoencoder approach with both losses playing an import role.

Number of Anchors We train our method for different anchor counts A with a constant two-hour training budget per model. In Fig. 8, we observe a low sensitivity to the anchor count. Due to repeated random sampling over the course of training, even $A = 1$ outperforms the correspondence error of Diff3F. Ultimately, we opt for $A = 100$ in all our experiments, as it balances computation cost and matching performance well. Note that A is not used during inference.

6. Applications

We present additional downstream tasks that benefit from *surface-aware features* learned in Sec. 5.1.

6.1. Instance-based Part Segmentation

Following prior work [24], we segment a target shape by clustering features around centroids from K-means clustering of source-shape features. In Fig. 9, we demonstrate a transfer from a big cat to a human and see that unlike the Diff3F features, our *surface-aware features* disambiguate the limbs. In Fig. 1, we repeat this with centroids obtained

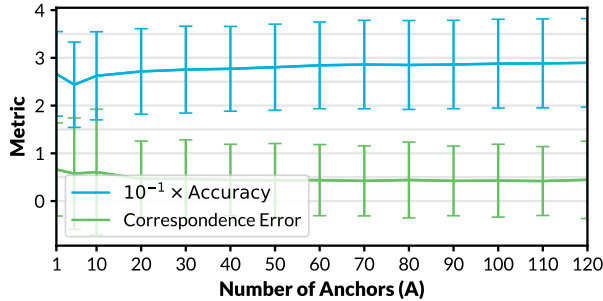


Figure 8. Ablation of anchor count A on *SHREC'19*. Our method improves upon Diff3F already from $A = 1$.

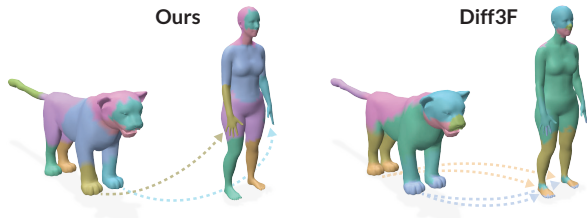


Figure 9. Ten k-means cluster centers from the big cat were used to segment the human. Our method successfully separates all limbs.

jointly from all *SHREC'19* and *TOSCA* samples. In contrast to Diff3F (see Appendix 10.2), our method successfully matches features across diverse shapes.

6.2. Pose Alignment

Our *surface-aware features* are also useful for the pose alignment of a kinematic model to another 3D shape. To this end, we establish point correspondences between shape pairs as in Sec. 5.1 and optimize the kinematic pose parameters to minimize point-to-point distances (see Appendix 9).

In Fig. 10, we align *SMPL^{eval}* to *SHREC'19*, and *SMAL^{eval}* to DeformingThings4D [45] animals. Benefiting from the robust instance separation, our method produces poses closer to the targets for both dense and sparse correspondences. See our video for a 3D shape animation obtained by aligning to a target shape sequence.

7. Discussion

Limitations and Future Work Our method inherits limitations connected to the extraction of the *base features*. Specifically, the extraction of Diff3F features [24] takes several minutes per mesh, and its vision model is sensitive to rendering artifacts. We expect that advances in rendering of point representations increase the applicability across representations [43]. Furthermore, objects that are isotropic both geometrically and semantically do not enable our method to establish a consistent partitioning of instanced components.

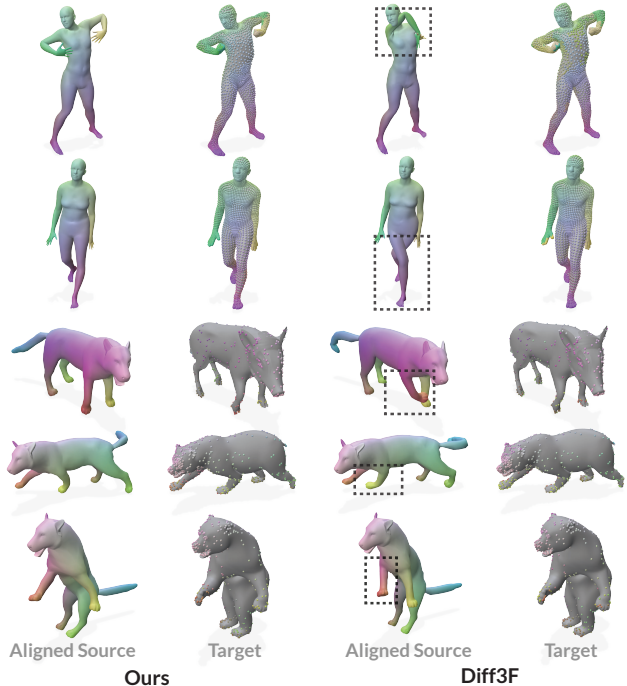


Figure 10. Pose alignment of a source shape (color) into the pose of a target (gray). The boxes highlight challenging areas handled well by our method. Top two rows densely fit to all target vertices, the bottom three only fit to 5 % of the target vertices (highlighted).

Hence, while our embedding separates human legs following the body’s notion of front and rear, it cannot do so for table legs. However, this is not an issue for applications such as shape morphing [74].

Beyond 3D alignment, our methodology could inspire 3D-to-2D pose estimation [42, 59], articulated 3D reconstruction [77, 86], automated rigging [84] or 2D-to-3D up-lifting [47, 61], where our features could support more view-consistent representations. Finally, an interesting topic for future research is the development of foundational features using massive datasets, such as Objaverse [18].

Conclusion We have introduced novel *surface-aware features* for 3D shape matching that disambiguate intraclass instances among semantic features derived from pre-trained 2D vision models. Our descriptors have proven effective in distinguishing instances of the same semantic class. They are capable of generalization even when trained on a limited number of 3D shapes. Furthermore, our contrastive loss facilitates easy integration in future methods without data labeling. Consequently, we perceive our method as a promising building block in the research landscape, aiming to exploit pre-trained 2D models for 3D tasks.

References

- [1] Ahmed Abdelreheem, Abdelrahman Eldesokey, Maks Ovsjanikov, and Peter Wonka. Zero-shot 3d shape correspondence. In *SIGGRAPH Asia 2023 Conference Papers*, pages 1–11, 2023. 2
- [2] Shir Amir, Yossi Gandelsman, Shai Bagon, and Tali Dekel. Deep vit features as dense visual descriptors. *arXiv preprint arXiv:2112.05814*, 2(3):4, 2021. 2
- [3] Jason Ansel, Edward Yang, Horace He, Natalia Gimelshein, Animesh Jain, Michael Voznesensky, Bin Bao, Peter Bell, David Berard, Evgeni Burovski, et al. Pytorch 2: Faster machine learning through dynamic python bytecode transformation and graph compilation. In *Proceedings of the 29th ACM International Conference on Architectural Support for Programming Languages and Operating Systems, Volume 2*, pages 929–947, 2024. 4
- [4] Souhaib Attaiki, Lei Li, and Maks Ovsjanikov. Generalizable local feature pre-training for deformable shape analysis. In *Proceedings of the IEEE/CVF Conference on Computer Vision and Pattern Recognition*, pages 13650–13661, 2023. 2
- [5] Mathieu Aubry, Ulrich Schlickewei, and Daniel Cremers. The wave kernel signature: A quantum mechanical approach to shape analysis. In *2011 IEEE international conference on computer vision workshops (ICCV workshops)*, pages 1626–1633. IEEE, 2011. 1, 2
- [6] Jimmy Lei Ba, Jamie Ryan Kiros, and Geoffrey E Hinton. Layer normalization. *arXiv preprint arXiv:1607.06450*, 2016. 4
- [7] Paul J Besl and Neil D McKay. Method for registration of 3-d shapes. In *Sensor fusion IV: control paradigms and data structures*, pages 586–606. Spie, 1992. 2
- [8] Alexander M Bronstein, Michael M Bronstein, and Ron Kimmel. *Numerical geometry of non-rigid shapes*. Springer Science & Business Media, 2008. 4, 5
- [9] Benedict J Brown and Szymon Rusinkiewicz. Global non-rigid alignment of 3-d scans. *ACM Transactions on Graphics (TOG)*, 26(3):21–es, 2007. 2
- [10] Mathilde Caron, Piotr Bojanowski, Armand Joulin, and Matthijs Douze. Deep clustering for unsupervised learning of visual features. In *Proceedings of the European conference on computer vision (ECCV)*, pages 132–149, 2018. 2
- [11] Mathilde Caron, Ishan Misra, Julien Mairal, Priya Goyal, Piotr Bojanowski, and Armand Joulin. Unsupervised learning of visual features by contrasting cluster assignments. *Advances in neural information processing systems*, 33:9912–9924, 2020. 2
- [12] Mathilde Caron, Hugo Touvron, Ishan Misra, Hervé Jégou, Julien Mairal, Piotr Bojanowski, and Armand Joulin. Emerging properties in self-supervised vision transformers. In *Proceedings of the IEEE/CVF international conference on computer vision*, pages 9650–9660, 2021. 2, 3
- [13] Ting Chen, Simon Kornblith, Mohammad Norouzi, and Geoffrey Hinton. A simple framework for contrastive learning of visual representations. In *International conference on machine learning*, pages 1597–1607. Pmlr, 2020. 2
- [14] Zhangquan Chen, Puhua Jiang, and Ruqi Huang. Dv-matcher: Deformation-based non-rigid point cloud matching guided by pre-trained visual features. *arXiv preprint arXiv:2408.08568v2*, 2025. 2, 4, 7, 1
- [15] Sumit Chopra, Raia Hadsell, and Yann LeCun. Learning a similarity metric discriminatively, with application to face verification. In *2005 IEEE computer society conference on computer vision and pattern recognition (CVPR'05)*, pages 539–546. IEEE, 2005. 2
- [16] Etienne Corman, Maks Ovsjanikov, and Antonin Chambolle. Supervised descriptor learning for non-rigid shape matching. In *European conference on computer vision*, pages 283–298. Springer, 2014. 2
- [17] Keenan Crane, Clarisse Weischedel, and Max Wardetzky. The heat method for distance computation. *Communications of the ACM*, 60(11):90–99, 2017. 4
- [18] Matt Deitke, Ruoshi Liu, Matthew Wallingford, Huong Ngo, Oscar Michel, Aditya Kusupati, Alan Fan, Christian Laforte, Vikram Voleti, Samir Yitzhak Gadre, et al. Objaverse-xl: A universe of 10m+ 3d objects. *Advances in Neural Information Processing Systems*, 36:35799–35813, 2023. 8
- [19] Haowen Deng, Tolga Birdal, and Slobodan Ilic. Ppf-foldnet: Unsupervised learning of rotation invariant 3d local descriptors. In *Proceedings of the European conference on computer vision (ECCV)*, pages 602–618, 2018. 2
- [20] Haowen Deng, Tolga Birdal, and Slobodan Ilic. Ppfnet: Global context aware local features for robust 3d point matching. In *Proceedings of the IEEE conference on computer vision and pattern recognition*, pages 195–205, 2018.
- [21] Jiacheng Deng, Chuxin Wang, Jiahao Lu, Jianfeng He, Tianzhu Zhang, Jiyang Yu, and Zhe Zhang. Se-or-net: Self-ensembling orientation-aware network for unsupervised point cloud shape correspondence. In *Proceedings of the IEEE/CVF Conference on Computer Vision and Pattern Recognition*, pages 5364–5373, 2023. 2, 3, 4, 5
- [22] Theo Deprelle, Thibault Groueix, Matthew Fisher, Vladimir Kim, Bryan Russell, and Mathieu Aubry. Learning elementary structures for 3d shape generation and matching. *Advances in Neural Information Processing Systems*, 32, 2019. 2
- [23] Nicolas Donati, Abhishek Sharma, and Maks Ovsjanikov. Deep geometric functional maps: Robust feature learning for shape correspondence. In *Proceedings of the IEEE/CVF Conference on Computer Vision and Pattern Recognition*, pages 8592–8601, 2020. 2, 4
- [24] Niladri Shekhar Dutt, Sanjeev Muralikrishnan, and Niloy J Mitra. Diffusion 3d features (diff3f): Decorating untextured shapes with distilled semantic features. In *Proceedings of the IEEE/CVF Conference on Computer Vision and Pattern Recognition*, pages 4494–4504, 2024. 2, 3, 4, 5, 7, 8, 1
- [25] Roberto M Dyke, Yu-Kun Lai, Paul L Rosin, Stefano Zappalà, Seana Dykes, Daoliang Guo, Kun Li, Riccardo Marin, Simone Melzi, and Jingyu Yang. Shrec’20: Shape correspondence with non-isometric deformations. *Computers & Graphics*, 92:28–43, 2020. 4
- [26] Marvin Eisenberger, Zorah Lahner, and Daniel Cremers. Smooth shells: Multi-scale shape registration with functional

- maps. In *Proceedings of the IEEE/CVF Conference on Computer Vision and Pattern Recognition*, pages 12265–12274, 2020. 2
- [27] Marvin Eisenberger, Aysim Toker, Laura Leal-Taixé, and Daniel Cremers. Deep shells: Unsupervised shape correspondence with optimal transport. *Advances in Neural Information Processing Systems*, 33:10491–10502, 2020. 2
- [28] Gil Elbaz, Tamar Avraham, and Anath Fischer. 3d point cloud registration for localization using a deep neural network auto-encoder. In *Proceedings of the IEEE conference on computer vision and pattern recognition*, pages 4631–4640, 2017. 2
- [29] Stefan Elfving, Eiji Uchibe, and Kenji Doya. Sigmoid-weighted linear units for neural network function approximation in reinforcement learning. *Neural networks*, 107:3–11, 2018. 4
- [30] Michael Fischer, Zhengqin Li, Thu Nguyen-Phuoc, Aljaz Bozic, Zhao Dong, Carl Marshall, and Tobias Ritschel. Nerf analogies: Example-based visual attribute transfer for nerfs. In *Proceedings of the IEEE/CVF Conference on Computer Vision and Pattern Recognition*, pages 4640–4650, 2024. 2
- [31] Martin A Fischler and Robert C Bolles. Random sample consensus: a paradigm for model fitting with applications to image analysis and automated cartography. *Communications of the ACM*, 24(6):381–395, 1981. 2
- [32] Dvir Ginzburg and Dan Raviv. Cyclic functional mapping: Self-supervised correspondence between non-isometric deformable shapes. In *Computer Vision—ECCV 2020: 16th European Conference, Glasgow, UK, August 23–28, 2020, Proceedings, Part V 16*, pages 36–52. Springer, 2020. 2
- [33] Zan Gojcic, Caifa Zhou, Jan D Wegner, and Andreas Wieser. The perfect match: 3d point cloud matching with smoothed densities. In *Proceedings of the IEEE/CVF conference on computer vision and pattern recognition*, pages 5545–5554, 2019. 2
- [34] Bingchen Gong, Diego Gomez, Abdullah Hamdi, Abdelrahman Eldesokey, Ahmed Abdelreheem, Peter Wonka, and Maks Ovsjanikov. Zerokey: Point-level reasoning and zero-shot 3d keypoint detection from large language models. *arXiv preprint arXiv:2412.06292*, 2024. 2
- [35] Thibault Groueix, Matthew Fisher, Vladimir G Kim, Bryan C Russell, and Mathieu Aubry. 3d-coded: 3d correspondences by deep deformation. In *Proceedings of the european conference on computer vision (ECCV)*, pages 230–246, 2018. 2, 4, 5
- [36] Kan Guo, Dongqing Zou, and Xiaowu Chen. 3d mesh labeling via deep convolutional neural networks. *ACM Transactions on Graphics (TOG)*, 35(1):1–12, 2015. 2
- [37] Raia Hadsell, Sumit Chopra, and Yann LeCun. Dimensionality reduction by learning an invariant mapping. In *2006 IEEE computer society conference on computer vision and pattern recognition (CVPR’06)*, pages 1735–1742. IEEE, 2006. 2
- [38] Oshri Halimi, Or Litany, Emanuele Rodola, Alex M Bronstein, and Ron Kimmel. Unsupervised learning of dense shape correspondence. In *Proceedings of the IEEE/CVF Conference on Computer Vision and Pattern Recognition*, pages 4370–4379, 2019. 2
- [39] Kaiming He, Xiangyu Zhang, Shaoqing Ren, and Jian Sun. Deep residual learning for image recognition. In *Proceedings of the IEEE conference on computer vision and pattern recognition*, pages 770–778, 2016. 4
- [40] Kaiming He, Haoqi Fan, Yuxin Wu, Saining Xie, and Ross Girshick. Momentum contrast for unsupervised visual representation learning. In *Proceedings of the IEEE/CVF conference on computer vision and pattern recognition*, pages 9729–9738, 2020. 2
- [41] Puhua Jiang, Mingze Sun, and Ruqi Huang. Neural intrinsic embedding for non-rigid point cloud matching. In *Proceedings of the IEEE/CVF Conference on Computer Vision and Pattern Recognition*, pages 21835–21845, 2023. 3, 7, 1
- [42] Angjoo Kanazawa, Michael J Black, David W Jacobs, and Jitendra Malik. End-to-end recovery of human shape and pose. In *Proceedings of the IEEE conference on computer vision and pattern recognition*, pages 7122–7131, 2018. 8
- [43] Bernhard Kerbl, Georgios Kopanas, Thomas Leimkühler, and George Drettakis. 3d gaussian splatting for real-time radiance field rendering. *ACM Trans. Graph.*, 42(4):139–1, 2023. 8
- [44] Itai Lang, Dvir Ginzburg, Shai Avidan, and Dan Raviv. Dpc: Unsupervised deep point correspondence via cross and self construction. In *2021 International Conference on 3D Vision (3DV)*, pages 1442–1451. IEEE, 2021. 2, 4, 5
- [45] Yang Li, Hikari Takehara, Takafumi Taketomi, Bo Zheng, and Matthias Nießner. 4dcomplete: Non-rigid motion estimation beyond the observable surface. In *Proceedings of the IEEE/CVF International Conference on Computer Vision*, pages 12706–12716, 2021. 8
- [46] Or Litany, Tal Remez, Emanuele Rodola, Alex Bronstein, and Michael Bronstein. Deep functional maps: Structured prediction for dense shape correspondence. In *Proceedings of the IEEE international conference on computer vision*, pages 5659–5667, 2017. 2
- [47] Ruoshi Liu, Rundi Wu, Basile Van Hoorick, Pavel Tokmakov, Sergey Zakharov, and Carl Vondrick. Zero-1-to-3: Zero-shot one image to 3d object. In *Proceedings of the IEEE/CVF international conference on computer vision*, pages 9298–9309, 2023. 8
- [48] Matthew Loper, Naureen Mahmood, Javier Romero, Gerard Pons-Moll, and Michael J Black. Smpl: A skinned multi-person linear model. In *Seminal Graphics Papers: Pushing the Boundaries, Volume 2*, pages 851–866. 2023. 5
- [49] Ilya Loshchilov and Frank Hutter. Decoupled weight decay regularization. *arXiv preprint arXiv:1711.05101*, 2017. 4
- [50] Weixin Lu, Guowei Wan, Yao Zhou, Xiangyu Fu, Pengfei Yuan, and Shiyu Song. Deepvcv: An end-to-end deep neural network for point cloud registration. In *Proceedings of the IEEE/CVF international conference on computer vision*, pages 12–21, 2019. 2
- [51] Grace Luo, Lisa Dunlap, Dong Huk Park, Aleksander Holynski, and Trevor Darrell. Diffusion hyperfeatures: Searching through time and space for semantic correspondence. *Advances in Neural Information Processing Systems*, 36: 47500–47510, 2023. 1
- [52] Naureen Mahmood, Nima Ghorbani, Nikolaus F Troje, Gerard Pons-Moll, and Michael J Black. Amass: Archive

- of motion capture as surface shapes. In *Proceedings of the IEEE/CVF international conference on computer vision*, pages 5442–5451, 2019. 5
- [53] Simone Melzi, Riccardo Marin, Emanuele Rodolà, Umberto Castellani, Jing Ren, Adrien Poulernard, P Ovsjanikov, et al. Shrec’19: matching humans with different connectivity. In *Eurographics Workshop on 3D Object Retrieval*, pages 1–8. The Eurographics Association, 2019. 4
- [54] Facundo Mémoli and Guillermo Sapiro. A theoretical and computational framework for isometry invariant recognition of point cloud data. *Foundations of Computational Mathematics*, 5:313–347, 2005. 2
- [55] Luca Morreale, Noam Aigerman, Vladimir G Kim, and Niloy J Mitra. Neural semantic surface maps. In *Computer Graphics Forum*, page e15005. Wiley Online Library, 2024. 2
- [56] Aaron van den Oord, Yazhe Li, and Oriol Vinyals. Representation learning with contrastive predictive coding. *arXiv preprint arXiv:1807.03748*, 2018. 2
- [57] Maxime Oquab, Timothée Darcet, Théo Moutakanni, Huy V. Vo, Marc Szafraniec, Vasil Khalidov, Pierre Fernandez, Daniel HAZIZA, Francisco Massa, Alaaeldin El-Nouby, Mido Assran, Nicolas Ballas, Wojciech Galuba, Russell Howes, Po-Yao Huang, Shang-Wen Li, Ishan Misra, Michael Rabbat, Vasu Sharma, Gabriel Synnaeve, Hu Xu, Herve Jegou, Julien Mairal, Patrick Labatut, Armand Joulin, and Piotr Bojanowski. DINOv2: Learning robust visual features without supervision. *Transactions on Machine Learning Research*, 2024. Featured Certification. 2, 3
- [58] Maks Ovsjanikov, Mirela Ben-Chen, Justin Solomon, Adrian Butscher, and Leonidas Guibas. Functional maps: a flexible representation of maps between shapes. *ACM Transactions on Graphics (ToG)*, 31(4):1–11, 2012. 2, 3
- [59] Sida Peng, Yuan Liu, Qixing Huang, Xiaowei Zhou, and Hujun Bao. Pvnnet: Pixel-wise voting network for 6dof pose estimation. In *Proceedings of the IEEE/CVF conference on computer vision and pattern recognition*, pages 4561–4570, 2019. 8
- [60] Boris T Polyak and Anatoli B Juditsky. Acceleration of stochastic approximation by averaging. *SIAM journal on control and optimization*, 30(4):838–855, 1992. 4
- [61] Ben Poole, Ajay Jain, Jonathan T Barron, and Ben Mildenhall. Dreamfusion: Text-to-3d using 2d diffusion. *arXiv preprint arXiv:2209.14988*, 2022. 8
- [62] Alec Radford, Jong Wook Kim, Chris Hallacy, Aditya Ramesh, Gabriel Goh, Sandhini Agarwal, Girish Sastry, Amanda Askell, Pamela Mishkin, Jack Clark, et al. Learning transferable visual models from natural language supervision. In *International conference on machine learning*, pages 8748–8763. PmLR, 2021. 2
- [63] E Rodolà, M Moeller, D Cremers, et al. Point-wise map recovery and refinement from functional correspondence. In *VMV 2015-Vision, Modeling and Visualization*, pages 25–32. Eurographics Association, 2015. 2
- [64] Robin Rombach, Andreas Blattmann, Dominik Lorenz, Patrick Esser, and Björn Ommer. High-resolution image synthesis with latent diffusion models. In *Proceedings of the IEEE/CVF conference on computer vision and pattern recognition*, pages 10684–10695, 2022. 2, 3
- [65] Jean-Michel Roufosse, Abhishek Sharma, and Maks Ovsjanikov. Unsupervised deep learning for structured shape matching. In *Proceedings of the IEEE/CVF International Conference on Computer Vision*, pages 1617–1627, 2019. 2
- [66] Florian Schroff, Dmitry Kalenichenko, and James Philbin. Facenet: A unified embedding for face recognition and clustering. In *Proceedings of the IEEE conference on computer vision and pattern recognition*, pages 815–823, 2015. 2
- [67] Gil Shamai and Ron Kimmel. Geodesic distance descriptors. In *Proceedings of the IEEE Conference on Computer Vision and Pattern Recognition*, pages 6410–6418, 2017. 2
- [68] Nicholas Sharp, Keenan Crane, et al. Geometrycentral: A modern c++ library of data structures and algorithms for geometry processing. 2019. 4
- [69] Nicholas Sharp et al. Polyscope, 2019. www.polyscope.run. 4
- [70] Aleksandar Shtedritski, Christian Rupprecht, and Andrea Vedaldi. Shic: Shape-image correspondences with no key-point supervision. In *European Conference on Computer Vision*, pages 129–145. Springer, 2024. 2
- [71] Olga Sorkine and Marc Alexa. As-rigid-as-possible surface modeling. In *Symposium on Geometry processing*, pages 109–116. Citeseer, 2007. 2
- [72] Jian Sun, Maks Ovsjanikov, and Leonidas Guibas. A concise and provably informative multi-scale signature based on heat diffusion. In *Computer graphics forum*, pages 1383–1392. Wiley Online Library, 2009. 1, 2
- [73] Mingze Sun, Shiwei Mao, Puhua Jiang, Maks Ovsjanikov, and Ruqi Huang. Spatially and spectrally consistent deep functional maps. In *Proceedings of the IEEE/CVF International Conference on Computer Vision*, pages 14497–14507, 2023. 2
- [74] Mingze Sun, Chen Guo, Puhua Jiang, Shiwei Mao, Yurun Chen, and Ruqi Huang. Srif: Semantic shape registration empowered by diffusion-based image morphing and flow estimation. In *SIGGRAPH Asia 2024 Conference Papers*, pages 1–11, 2024. 8
- [75] Luming Tang, Menglin Jia, Qianqian Wang, Cheng Perng Phoo, and Bharath Hariharan. Emergent correspondence from image diffusion. *Advances in Neural Information Processing Systems*, 36:1363–1389, 2023. 1, 3
- [76] Federico Tombari, Samuele Salti, and Luigi Di Stefano. Unique signatures of histograms for local surface description. In *Computer Vision—ECCV 2010: 11th European Conference on Computer Vision, Heraklion, Crete, Greece, September 5–11, 2010, Proceedings, Part III 11*, pages 356–369. Springer, 2010. 1, 2
- [77] Lukas Uzolas, Elmar Eisemann, and Petr Kellnhofer. Template-free articulated neural point clouds for reusable view synthesis. *Advances in Neural Information Processing Systems*, 36:31621–31637, 2023. 8
- [78] Lukas Uzolas, Elmar Eisemann, and Petr Kellnhofer. Motiondreamer: Zero-shot 3d mesh animation from video diffusion models. *arXiv preprint arXiv:2405.20155*, 2024. 2

- [79] Yue Wang and Justin M Solomon. Deep closest point: Learning representations for point cloud registration. In *Proceedings of the IEEE/CVF international conference on computer vision*, pages 3523–3532, 2019. [2](#)
- [80] Kilian Q Weinberger and Lawrence K Saul. Distance metric learning for large margin nearest neighbor classification. *Journal of machine learning research*, 10(2), 2009. [2](#)
- [81] Thomas Wimmer, Peter Wonka, and Maks Ovsjanikov. Back to 3d: Few-shot 3d keypoint detection with back-projected 2d features. In *Proceedings of the IEEE/CVF Conference on Computer Vision and Pattern Recognition*, pages 4154–4164, 2024. [1](#), [2](#)
- [82] Zhirong Wu, Yuanjun Xiong, Stella X Yu, and Dahua Lin. Unsupervised feature learning via non-parametric instance discrimination. In *Proceedings of the IEEE conference on computer vision and pattern recognition*, pages 3733–3742, 2018. [2](#)
- [83] Qianwei Xia, Juyong Zhang, Zheng Fang, Jin Li, Mingyue Zhang, Bailin Deng, and Ying He. Geodesicembedding (ge): a high-dimensional embedding approach for fast geodesic distance queries. *IEEE Transactions on Visualization and Computer Graphics*, 28(12):4930–4939, 2021. [2](#)
- [84] Zhan Xu, Yang Zhou, Evangelos Kalogerakis, Chris Landreth, and Karan Singh. Rignet: neural rigging for articulated characters. *ACM Transactions on Graphics (TOG)*, 39(4):58–1, 2020. [8](#)
- [85] Jiaolong Yang, Hongdong Li, Dylan Campbell, and Yunde Jia. Go-icp: A globally optimal solution to 3d icp point-set registration. *IEEE transactions on pattern analysis and machine intelligence*, 38(11):2241–2254, 2015. [2](#)
- [86] Chun-Han Yao, Wei-Chih Hung, Yuanzhen Li, Michael Rubinstein, Ming-Hsuan Yang, and Varun Jampani. Lassie: Learning articulated shapes from sparse image ensemble via 3d part discovery. *Advances in Neural Information Processing Systems*, 35:15296–15308, 2022. [8](#)
- [87] Zi Jian Yew and Gim Hee Lee. 3dfeat-net: Weakly supervised local 3d features for point cloud registration. In *Proceedings of the European conference on computer vision (ECCV)*, pages 607–623, 2018. [2](#)
- [88] Andy Zeng, Shuran Song, Matthias Nießner, Matthew Fisher, Jianxiong Xiao, and Thomas Funkhouser. 3dmatch: Learning local geometric descriptors from rgb-d reconstructions. In *Proceedings of the IEEE conference on computer vision and pattern recognition*, pages 1802–1811, 2017. [2](#)
- [89] Yiming Zeng, Yue Qian, Zhiyu Zhu, Junhui Hou, Hui Yuan, and Ying He. Cornet3d: Unsupervised end-to-end learning of dense correspondence for 3d point clouds. In *Proceedings of the IEEE/CVF Conference on Computer Vision and Pattern Recognition*, pages 6052–6061, 2021. [2](#)
- [90] Junyi Zhang, Charles Herrmann, Junhwa Hur, Luisa Polania Cabrera, Varun Jampani, Deqing Sun, and Ming-Hsuan Yang. A tale of two features: Stable diffusion complements dino for zero-shot semantic correspondence. *Advances in Neural Information Processing Systems*, 36:45533–45547, 2023. [2](#), [3](#)
- [91] Junyi Zhang, Charles Herrmann, Junhwa Hur, Eric Chen, Varun Jampani, Deqing Sun, and Ming-Hsuan Yang. Telling left from right: Identifying geometry-aware semantic correspondence. In *Proceedings of the IEEE/CVF Conference on Computer Vision and Pattern Recognition*, pages 3076–3085, 2024. [1](#), [2](#), [4](#)
- [92] Junyi Zhang, Charles Herrmann, Junhwa Hur, Luisa Polania Cabrera, Varun Jampani, Deqing Sun, and Ming-Hsuan Yang. A tale of two features: Stable diffusion complements dino for zero-shot semantic correspondence. *Advances in Neural Information Processing Systems*, 36, 2024. [1](#)
- [93] Lvmin Zhang, Anyi Rao, and Maneesh Agrawala. Adding conditional control to text-to-image diffusion models. In *Proceedings of the IEEE/CVF international conference on computer vision*, pages 3836–3847, 2023. [3](#)
- [94] Silvia Zuffi, Angjoo Kanazawa, David W Jacobs, and Michael J Black. 3d menagerie: Modeling the 3d shape and pose of animals. In *Proceedings of the IEEE conference on computer vision and pattern recognition*, pages 6365–6373, 2017. [4](#), [5](#)

Surface-Aware Distilled 3D Semantic Features

Supplementary Material

8. Additional implementation details

We provide additional details to reproduce our experiments. We will make the code publicly available upon publication.

8.1. Diff3F

We use the authors’ code to compute the Diff3F features [24] for our *base features* and as a baseline method for comparison.

Since we observed that the camera poses used for sampling in the *TOSCA* dataset are biased towards a specific up-direction, we modified the code to flip the coordinate system for only this dataset. Doing so yields $\approx 10\%$ increase in correspondence accuracy in *TOSCA* for both our method and the Diff3F baseline, when compared to the numbers reported in the Diff3F paper [24]. An alternative solution could be a modification of the camera sampling algorithm itself.

8.2. Ablations

Utilizing the geodesic distance as a supervision signal for embeddings has been explored in related works [14, 41]. However, in our ablations, we show that we achieve superior results with our formulation. In this section, we discuss the key differences.

Relative Geodesic Loss (RGL) Based on two points, v_p and v_q , the Relative Geodesic Loss [41] minimizes the difference between the geodesic distance d^S and the *Euclidean* embedding distance d^E of those two points, relative to the surface distance:

$$L_{RGL} = \sum_i \sum_{(p,q) \in S_i} \frac{|d_i^E(v_p, v_q) - d^S(v_p, v_q)|^2}{d^S(v_p, v_q)^2}. \quad (4)$$

The normalization term is introduced to prioritize local distance preservation. We do not utilize this normalization term, as the *base features* struggle to disambiguate samples that are far away on the surface but close in feature space, such as “left hand” and “right hand”.

Naive Geodesic Loss (NGL) *NGL* is discussed in [41] but not used for training, as the authors state that it might hamper local distance preservation. Indeed, in our ablations, it achieves worse results in terms of correspondence accuracy when compared to *RGL*. It is identical to *RGL* but it omits the normalization term:

$$L_{NGL} = \sum_i \sum_{(p,q) \in S_i \in [n_i]^2} |d_i^E(v_p, v_q) - d^S(v_p, v_q)|^2 \quad (5)$$

While not actually utilized in their work, *NGL* is closest to our formulation. However, our choice of a hyperspherical rather than Euclidean embedding space in combination with our autoencoder setup achieves notably better results.

Geometric Similarity Loss (GSL) A concurrent work proposes to maximize the *local angular similarity* between geodesic distances and *Euclidean* feature vectors for a set of neighbors for each point [14]. Crucially, the similarity is only maximized for a set of k point pairs nearest in the embedding space. The loss is a cosine metric between a vector of geodesic distances $\mathbf{m}_i \in \mathbb{R}^k$ and a vector of *Euclidean* embedding distances $\mathbf{d}_i \in \mathbb{R}^k$:

$$\mathcal{L}_{GSL} = \frac{1}{N} \sum_{i=1}^N \left(1 - \frac{\mathbf{d}_i \cdot \mathbf{m}_i}{\|\mathbf{d}_i\| \|\mathbf{m}_i\|} \right). \quad (6)$$

This restricts *GSL* supervision to a fixed neighborhood size and potentially limits disambiguation of features that are close in feature space but not among the k nearest neighbors. In contrast, our method follows a global approach by sampling anchors based on a furthest point sampling.

Conclusion Our method differs from recent works utilizing vision-based features for 3D shape matching in three main aspects: 1) we follow a global approach when enforcing distances in the embedding space; 2) our embedding space is hyperspherical and it only encodes angular information; 3) in context of the whole pipeline, we solely rely on intrinsic properties.

9. Pose Alignment

We establish correspondences based on ϕ , such that each point \mathbf{x}_i^S in the source shape is assigned a target point \mathbf{x}_i^T in the target shape (see Sec. 3). We then align the source to the target by minimizing the following L1 loss:

$$\mathcal{L}_{point} = \frac{1}{N} \sum_i^N \|\mathbf{x}_i^S - \mathbf{x}_i^T\|_1. \quad (7)$$

For the first half of the optimization, we only optimize the root rotation \mathbf{R} , root translation \mathbf{t} , and scale s , which roughly aligns the meshes. In the second half, we additionally optimize the rotation \mathbf{R}_b of each kinematic bone b . The parameters are optimized based on a gradient-descent for 4000 iterations, which takes approximately 30 seconds for a static pose.

Furthermore, we found it beneficial to use an as-rigid-as-possible regularization [71], which penalizes the deviation between the initial edge lengths of the mesh δ_e^{init} and the current edge length δ_e for each edge e :

$$\mathcal{L}_{arap} = \frac{1}{E} \sum_e |\delta_e^{init} - \delta_e|. \quad (8)$$

When fitting an animation as a pose sequence, we optimize the pose parameters for each time step t . Furthermore, we apply pointwise temporal smoothing for neighboring frames:

$$\mathcal{L}_{smooth} = \frac{1}{N(T-1)} \sum_t \sum_i \|\mathbf{x}_{i,t}^S - \mathbf{x}_{i,t+1}^S\|_2^2. \quad (9)$$

The final loss is $\mathcal{L}_{pose} = w_p \mathcal{L}_{point} + w_a \mathcal{L}_{arap} + w_s \mathcal{L}_{smooth}$ with $w_p = w_a = w_s = 1$ for animations and $w_s = 0$ otherwise.

10. Additional results

10.1. Qualitative Results on SHREC'20

Fig. 11 presents additional results for the *SHREC'20* dataset. As the dataset only provides ≈ 50 correspondences for each shape pair, we do display dense ground-truth labels. However, we find that our features generally produce smoother correspondences (e.g., bottom left) and a better separation of legs (e.g., second to last row on the right).

10.2. Clustering

Same as in Sec. 6.1, we obtain the centroids from all *SHREC'19* and *TOSCA* samples' features, but this time with the Diff3F. We use those centroids to segment a set of shapes. The results are shown in Fig. 12. While animal limbs and bodies are still assigned to the same cluster, limbs are not disambiguated and they are not assigned to the same clusters between humanoids and animals. Notably, this is not an issue with our *surface-aware* features in Fig. 1.

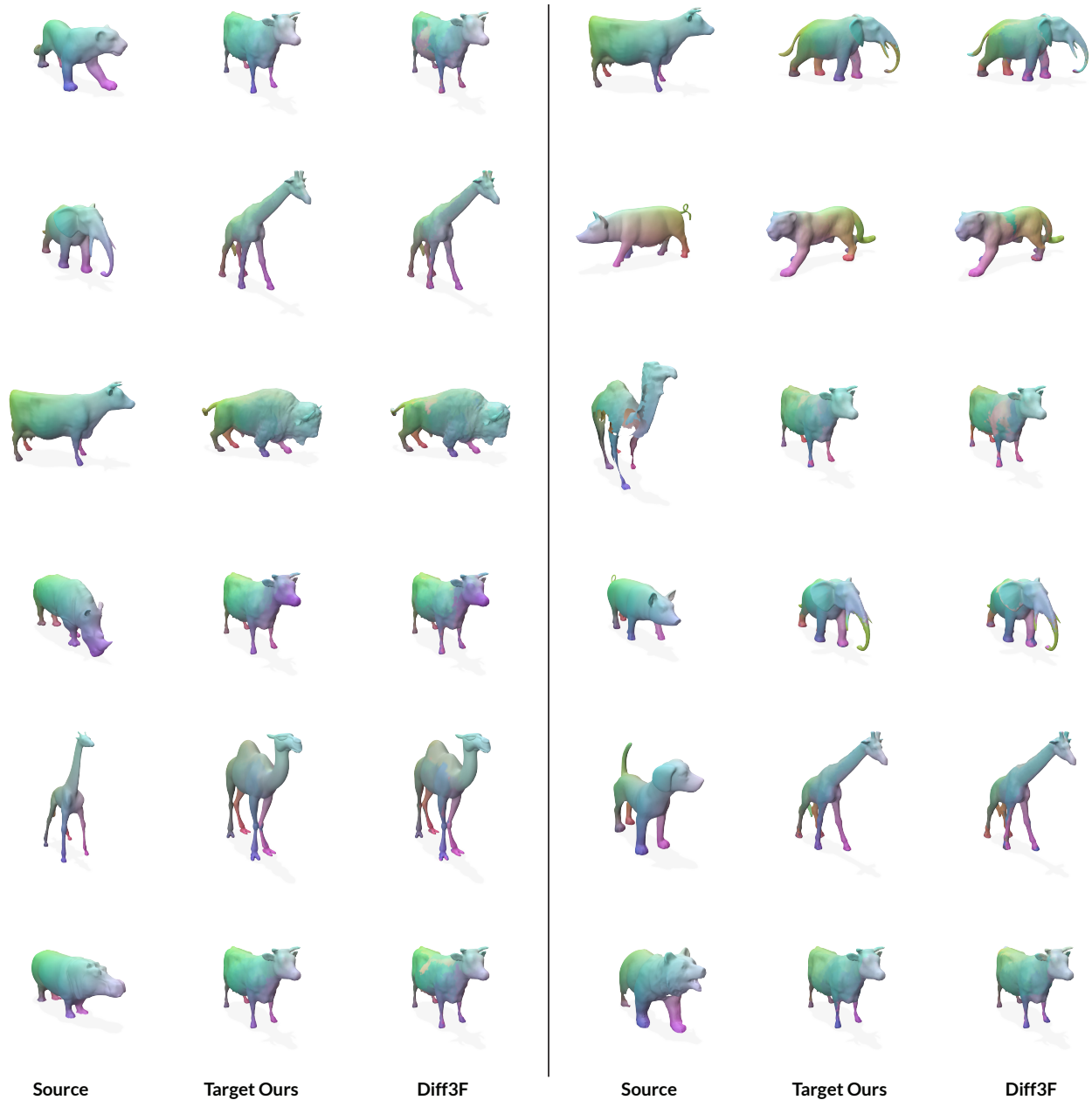


Figure 11. Qualitative results on *SHREC'20*. Our features result on average in more accurate smooth mapping between different limbs.



Figure 12. Reproduction of the clustering experiment shown in Fig. 1 but utilizing Diff3F features instead of our features. Notice the inconsistency of labeling across different shape categories as well as lack of separability between instanced components such as individual limbs.